Applied Thermal Engineering 257 (2024) 124281

Contents lists available at ScienceDirect

Applied Thermal Engineering

journal homepage: www.elsevier.com/locate/ate

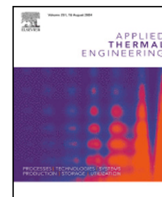

Research Paper

Modeling the thermal and hydrodynamic performance of grooved wick flat heat pipes

Callum Chhokar, Mahyar Ashouri, Majid Bahrami *

Laboratory for Alternative Energy Conversion (LAEC), School of Mechatronic Systems Engineering, Simon Fraser University, Burnaby, BC V3T 0A3, Canada

ARTICLE INFO

Keywords:
flat micro heat pipe
grooved wick
thin film evaporation
analytical model

ABSTRACT

A compact model is developed to predict the thermal and hydrodynamic performance of a flat heat pipe with a rectangular grooved wick. The present model relies on the analytical solution to the energy equation in the wall and an equivalent heat transfer coefficient predicted using a computationally efficient iterative method. This efficient iterative method can also provide a framework for modeling other grooved or porous wick heat pipes for which analytical or semi-analytical solutions to the wall conduction, fluid flow, and film equations exist. Compared to prior numerical tools, the present modeling approach is computationally efficient, making it compelling for use in parametric and optimization studies. Instead of numerically solving a set of coupled differential equations, the present model considers only analytical and semi-analytical solutions for evaporation and condensation heat transfer rates. The non-discretized nature of the present model allows computations on a typical workstation to be completed within seconds as opposed to the hours required for prevalent numerical tools. The present model accounts for varying liquid fill volumes, geometry, and interfacial properties, such as surface tension and contact angle. The present model closely agrees with published numerical and experimental results for wall temperatures and maximum heat transfer rates. Parametric studies, which vary wall thermal conductivity, water contact angle, and groove dimensions are conducted on a previously experimentally investigated heat pipe to demonstrate the present model's capabilities. The present model found that the maximum heat transfer rate of the heat pipe can be enhanced by about 15 and 20% by varying its wetting angle and groove dimensions, respectively.

1. Introduction

Traditional transistor scaling trends have enabled thermally unconstrained increases in computational power, prompting significant breakthroughs in transformative fields such as artificial intelligence (AI). However, these scaling trends have slowed recently, resulting in thermal constraints on high-performance computing and power electronics [1–4]. Advanced Micro Devices Inc. (AMD) reported that the thermal design powers (TDPs) of their server CPU and GPUs had risen at about 7% per year between 2006 and 2017 [5]. Industry roadmaps anticipate faster server CPU and GPU thermal design power gains, predicting them to double by 2030 [6], with the status quo ultimately reaching the 600 W set by Intel's newly released Data Center GPU Max 1550, formerly named Ponte Vecchio [7]. Thermal limitations are exacerbated in power electronics, where transistor and die-level heat fluxes are expected to reach a staggering 30 and $1\,\mathrm{kW\,cm^{-2}}$, respectively [2–4]. With the breakdown of traditional scaling trends and the emergence of thermal constraints on the computing power of electronics in transformative fields, it is apparent that there is a pressing need to improve existing thermal management solutions.

Introduced in 1984 by Cotter [8], flat micro heat pipes are prominent passive thermal management solutions that effectively distribute heat in the confined spaces of high-performance computing and power electronics devices. Established thermal limitations necessitate improved heat pipe thermal performance, notably elevated maximum heat transport rates and effective thermal conductivities. More recently, studies have investigated substrate-embedded architectures [9–12], intricate fractally-patterned wick structures [13–16], and nanofluids [17–20], to enhance the thermal management potential and thermal performance of two-phase heat spreaders, such as flat micro heat pipes. Fundamentally, enhancing thermal performance requires a comprehensive understanding of the heat and mass transport, mainly phase change phenomena and fluid flow (liquid and vapor), to optimize the design of the heat pipe, including the wick structure.

Several studies have modeled miniature and micro heat pipes. Babin et al. [21] numerically and experimentally investigated the steady-state performance of several wickless micro heat pipes. Their numerical

* Corresponding author.
E-mail address: mbahrami@sfu.ca (M. Bahrami).

https://doi.org/10.1016/j.applthermaleng.2024.124281
Received 13 May 2024; Received in revised form 23 August 2024; Accepted 28 August 2024
Available online 31 August 2024
1359-4311/© 2024 The Author(s). Published by Elsevier Ltd. This is an open access article under the CC BY license (http://creativecommons.org/licenses/by/4.0/).

Nomenclature

$\dot{m}'$	mass flow rate per unit length [$kg\,s^{-1}\,m^{-1}$]
$\dot{m}''$	mass flux [$kg\,s^{-1}\,m^{-2}$]
$\dot{Q}$	heat transfer rate [W]
$\dot{Q}'$	heat transfer rate per unit length [$W\,m^{-1}$]
$\hat{H}$	normalized height ratio
$\hat{W}$	normalized width ratio
Bi	Biot number = ht_w/k_w
Re	Reynolds number
A	dispersion constant [J]
a	coefficient defined in Eq. (27b) [$kg\,s^{-1}\,m^{-2}\,K^{-1}$]
b	coefficient defined in Eq. (27b) [$kg\,s^{-1}\,m^{-2}\,Pa^{-1}$]
D_h	hydraulic diameter [m]
f	friction factor
H	height [m]
h	heat transfer coefficient [$W\,m^{-2}\,K^{-1}$]
h_{fg}	latent heat [$J\,kg^{-1}$]
K	meniscus curvature [m^{-1}]
k	thermal conductivity [$W\,m^{-1}\,K^{-1}$]
L	length [m]
l	length of the meniscus region [m]
M	molecular weight [$kg\,mol^{-1}$]
N	total number of grooves
n	local coordinate normal to the groove wall [m]
p	pressure [Pa]
R	universal gas constant [$J\,mol^{-1}\,K^{-1}$]
r	radius [m]
s	local coordinate parallel to the groove wall [m]
T	temperature [K]
t	thickness [m]
u	axial velocity [$m\,s^{-1}$]
W	width [m]
w	transverse velocity [$m\,s^{-1}$]
x	axial coordinate [m]
y	cross-sectional coordinate [m]

Greek symbols

α	groove wall inclination angle [°]
δ	liquid film thickness [m]
ϵ	aspect ratio
γ_{lv}	liquid–vapor interfacial energy (surface tension) [$N\,m^{-1}$]
κ	curvature [m^{-1}]
μ	dynamic viscosity [Pa s]
ν	kinematic viscosity [$m^2\,s^{-1}$]
ρ	density [$kg\,m^{-3}$]
σ	accommodation coefficient
τ	shear stress [$N\,m^{-2}$]
θ	contact angle [°]

Subscripts

a	adiabatic
b	liquid block
c	condenser
cap	capillary
d	disjoining
e	evaporator
eff	effective
eq	equivalent
fin	groove fin
g	groove
in	input
l	liquid
lv	liquid–vapor
max	maximum
men	meniscus region
min	minimum
out	output
t	total
thin	evaporating thin film region
v	vapor
w	wall

model, validated by their experimental results, could predict the maximum heat transport rate and identified that the capillary limit was the predominant constraint. Wu and Peterson [22] developed a transient numerical model for a wickless micro heat pipe to predict its performance during startup or transient heat power inputs, validating their model with the steady-state experimental results of Babin et al. [21]. They concluded that the contact or wetting angle was critical in determining the maximum heat transport rate. Khrustalev and Faghri [23] developed a mathematical model for wickless triangular micro heat pipes, validating their results with the experimental results of Babin et al. [21]. Their model showed that the liquid–vapor interfacial shear stress, contact angle, and filling ratio influence the maximum heat transport rate. Additionally, they suggested a new cross-section for a flat micro heat pipe with noticeably more grooves. Subsequently, Khrustalev and Faghri [24,25] modeled and experimentally investigated flat micro heat pipes with axially grooved wicks. They found that groove geometry significantly influenced the maximum heat transport rate. Along with a mathematical model [24], they developed a convenient closed-form estimation of the maximum heat transport rate of flat micro heat pipes with rectangular grooved wicks [25]:

$$\dot{Q}_{max} = \frac{2h_{fg}\gamma_{lv}\cos\theta}{W_g L_{eff}} \left[(f\mathrm{Re})_v \frac{2\mu_v}{D_{h,v}^2 \rho_v H_v W_v} + (f\mathrm{Re})_l \frac{2\mu_l}{D_{h,l}^2 \rho_l N H_g W_g} \right]^{-1} \tag{1}$$

where $\dot{Q}_{max}$, h_{fg}, γ_{lv}, θ, L_{eff}, f, Re, μ, D_h, ρ, H, W, and N are the maximum heat transfer rate, latent heat, surface tension, contact angle, effective length, friction factor, Reynolds number, dynamic viscosity, hydraulic diameter, density, height, width, and number of grooves, respectively.

Although this closed-form estimation is convenient, it has been shown to substantially differ from experimental results [25]. At the cost of computational complexity, results that are more consistent with experimental results can be found using numerical modeling. High-fidelity numerical methods for heat pipes are relatively universal (i.e., applicable to many different geometries and wick structures) and well documented in the literature (e.g., [26–31]) but computationally costly. Gökçe et al. [30,31] reported that their detailed numerical modeling tools took hours to complete their computations on a modern workstation, even without considering the vapor flow. Other more

computationally efficient numerical tools exist but are typically heat pipe architecture-specific. Kim and Do et al. and Lefèvre et al. [32–34] used numerically solved mathematical models to predict the thermal and hydrodynamic performance of axially grooved cylindrical and flat heat pipes. Do et al. [33] used their model to optimize groove geometry, theoretically enhancing the maximum heat transport rate of the rectangular grooved wick flat heat pipe of Hopkins et al. [25] by about 20%. More recently, Saygan et al. [35] developed a computationally efficient, compact numerical model for rectangular grooved wick flat heat pipes that, unlike many prior models, could predict the vapor temperature. Saygan et al. [13] extended their model to consider fractal groove geometries. Their model was used to design a bifurcated grooved wick heat pipe exhibiting a 25% higher maximum heat transport rate than its straight groove counterpart. Their compact model did not resolve the vapor flow, neglecting viscous losses in the vapor core and entrainment losses at the liquid–vapor interface. These losses are crucial when considering thin-walled heat pipes with minimal vapor spacing (i.e., micro heat pipes).

Prasher and Zimmerman et al. [36,37] and Lips and Lefèvre [38,39] developed analytical models for heat pipes using conduction-based and coupled hydrodynamic-thermal approaches, respectively. These models considered an effective wick thermal conductivity, which can be estimated analytically [40,41], semi-empirically [42], or numerically [43]. These estimations are limiting, with the former considering non-evaporating saturated sintered powders and mesh structures and the latter two introducing applicability and computational concerns, respectively. Considering all the mentioned models, there is a need for a compact model for flat micro heat pipes with rectangular grooved wicks, which analytically (or semi-analytically) accounts for phase change phenomena and fluid flow (liquid and vapor) in its heat and mass transport modeling.

The present study develops a computationally efficient, compact mathematical model to predict the thermal and hydrodynamic performance of a flat micro heat pipe with a rectangular grooved wick. The present model considers pertinent parameters, including groove geometry, contact angle, and fill ratio, to list a few. To the authors' knowledge, this is the first heat pipe model in which wall temperatures, hydrodynamics, and phase change rates are solved simultaneously using analytical and semi-analytical solutions to the wall conduction, fluid flow (liquid and vapor), and film equations. Given the non-discretized nature of the present model, computations on most workstations can be completed within seconds instead of the hours required for prevalent numerical tools. The present model's flexible approach offers an efficient iterative method that can provide a framework for modeling other grooved or porous wick heat pipes for which analytical or semi-analytical solutions to the wall conduction, fluid flow (liquid and vapor), and film equations exist. Additionally, the present model solves for the maximum heat transfer rate by iteratively checking the maximum capillary pressure against the maximum governed by the Young–Laplace equation. The maximum capillary pressure, or maximum liquid–vapor pressure difference, is calculated by considering viscous and entrainment pressure losses in the grooved wick and vapor core. The model is validated with existing experimental wall temperature and maximum heat transfer rate data. Finally, parametric studies demonstrate the model's capability to enhance a heat pipe's maximum heat transfer rate and minimize thermal resistance.

2. Model development

A flat micro heat pipe with a rectangular grooved wick structure is considered, as schematically shown in Fig. 1. The heat pipe is assumed to have a constant vapor temperature, consistent with prior mathematical modeling [33]. Also, it is subject to uniform, balanced, steady-state heat transfer rates in the evaporator and condenser. As shown in Fig. 2, the heat pipe is thermally modeled as a flat plate. The flat plate has the exact dimensions of the heat pipe's wall (width, thickness, and length) and is subject to an identical heat transfer rate. A two-dimensional temperature distribution (along the axial direction and perpendicular to the wall) and a uniform, equivalent heat transfer coefficient are assumed. As such, the governing two-dimensional energy equation and its classical solution are [39,44]:

$$\frac{\partial^2 T}{\partial x^2}+\frac{\partial^2 T}{\partial y^2}=0 \tag{2}$$

$$T(x,y)-T_v=\frac{\dot{Q}_{in}t_w}{2W_t k_w}\sum_{m=1}^{\infty}A_m\frac{C_m\exp(B_m y)+D_m\exp(-B_m y)}{C_m\exp(B_m t_w)-D_m\exp(-B_m t_w)}\cos(B_m x) \tag{3a}$$

where T, T_v, $\dot{Q}_{in}$, W_t, t_w, and k_w are the wall temperature, vapor temperature, heat power input, total (outer) width, wall thickness, and wall thermal conductivity, respectively. As shown in Fig. 1, an overfilled heat pipe with a liquid block in the condenser is considered. The present model neglects heat transfer in the liquid block. As such, a corrected (shortened) condenser length is used to determine the coefficients A_m, B_m, C_m, and D_m:

$$A_m=\frac{2}{m^2\pi^2 t_w}\times\left[\frac{L_t-L_b}{L_e}\sin\left(m\pi\frac{L_e}{L_t-L_b}\right)+\frac{L_t-L_b}{L_c-L_b}\sin\left(m\pi\frac{L_t-L_c}{L_t-L_b}\right)\right] \tag{3b}$$

$$B_m=\frac{m\pi}{L_t-L_b},\qquad C_m=B_m t_w+\mathrm{Bi}_{eq},\qquad D_m=B_m t_w-\mathrm{Bi}_{eq} \tag{3c}$$

$$\mathrm{Bi}_{eq}=\frac{h_{eq}t_w}{k_w} \tag{3d}$$

where Bi_{eq} and h_{eq} are the equivalent Biot number and equivalent heat transfer coefficient, respectively. L_e, L_c, L_b, and L_t are the evaporator, condenser, liquid block, and total lengths, respectively. Using Eq. (3), the inner superheat or subcool is expressed as:

$$\Delta T(x,0)=T(x,0)-T_v=\frac{\dot{Q}_{in}t_w^2}{W_t k_w}\sum_{m=1}^{\infty}\frac{A_m B_m\cos(B_m x)}{C_m\exp(B_m t_w)-D_m\exp(-B_m t_w)} \tag{4}$$

2.1. Hydrodynamics

The liquid flow in the grooves is assumed to be one-dimensional, fully developed, and incompressible. As such, its velocity is related to its pressure gradient using conservation of momentum:

$$u_l(x)=-\frac{D_{h,l}^2}{2\mu_l(f\mathrm{Re})_l}\frac{\mathrm{d}p_l}{\mathrm{d}x} \tag{5}$$

where u_l and $\mathrm{d}p_l/\mathrm{d}x$ are the axial liquid velocity and pressure gradient, respectively. Schneider and DeVos suggested the following $(f\mathrm{Re})_l$ correlation for rectangular grooves [45]:

$$(f\mathrm{Re})_l=(f\mathrm{Re})_{l0}\left\{1+\frac{D_{h,l}}{12\mu_l\epsilon_g^2}\frac{\tau_{lv}}{u_v}\left|\frac{u_v}{u_l}\right|\left[1-1.971\exp\left(-\pi\epsilon_g\right)\right]\right\} \tag{6a}$$

where ϵ_g, τ_{lv}, and u_v are the groove height-to-width ratio, interfacial shear stress, and vapor velocity, respectively. $(f\mathrm{Re})_{l0}$ corresponds to the case of no vapor flow and is as follows:

$$(f\mathrm{Re})_{l0}=\frac{32\epsilon_g^2}{\left(1+2\epsilon_g\right)^2\left\{1/3-32\tanh\left(\pi\epsilon_g\right)/\left(\pi^5\epsilon_g\right)\right\}} \tag{6b}$$

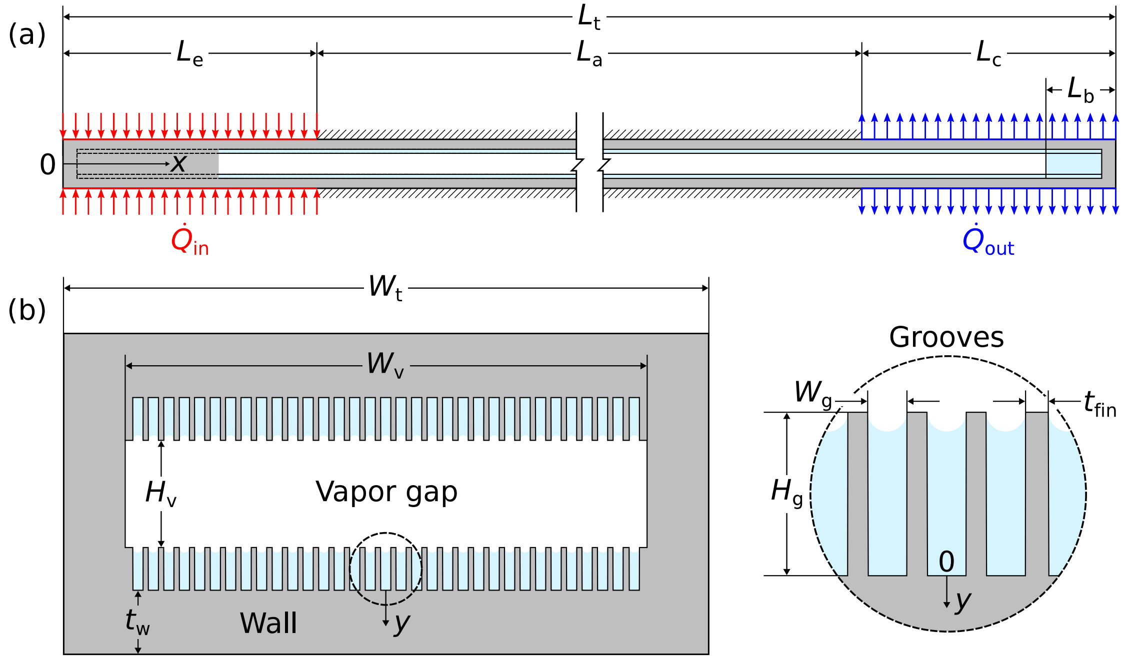

Fig. 1. Flat micro heat pipe with a grooved rectangular wick considered in this study: (a) lengthwise dimensions and considered boundary conditions, and (b) cross-sectional dimensions.

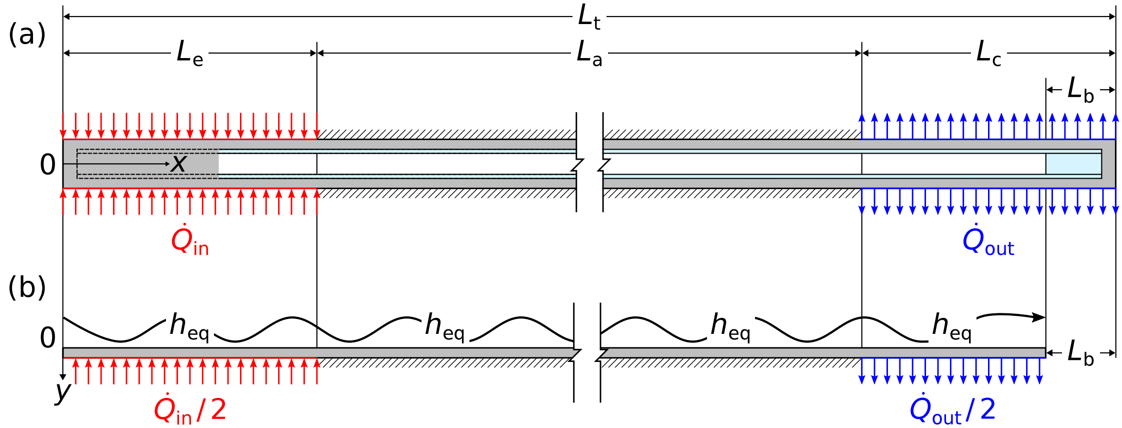

Fig. 2. Thermal modeling of the (a) flat micro heat pipe considered in this study as (b) a flat plate subject to balanced heat fluxes at both ends and an inner equivalent heat transfer coefficient.

Liquid velocity is negligible compared to vapor's, $u_v \gg u_l$ [46]. Thus, the liquid–vapor interfacial shear stress is determined using the classical shear stress equation for a rectangular duct, which is applied as follows [33,47]:

$$\frac{\tau_{lv}}{u_v} = \frac{48\mu_v}{\pi^2 W_v} \frac{\sum_{n=1}^{\infty}\left[(-1)^{n-1}/(2n-1)^2\right]\tanh\left[(2n-1)\pi\epsilon_v/2\right]}{\left\{1-(192/\pi^5)\,\epsilon_v^{-1}\sum_{n=1}^{\infty}(2n-1)^{-5}\tanh\left[(2n-1)\pi\epsilon_v/2\right]\right\}} \tag{6c}$$

where ϵ_v is the vapor core height-to-width ratio. The liquid velocity gradient is found from continuity:

$$\frac{du_l}{dx} = -\frac{2\mathrm{Bi}_{eq}(k_w/t_w)\,W_t\left[\Delta T(x,0)\right]}{\rho_l h_{fg} N H_g W_g} \tag{7}$$

Combining Eqs. (5) and (7) yields:

$$\begin{aligned}\frac{d^2 p_l}{dx^2} &= \frac{4\mu_l (f\mathrm{Re})_l \mathrm{Bi}_{eq}(k_w/t_w)\,W_t\left[\Delta T(x,0)\right]}{D_{h,l}^2\rho_l h_{fg} N H_g W_g} \\ &= \dot{Q}_{in}\left[\frac{4\mu_l (f\mathrm{Re})_l t_w \mathrm{Bi}_{eq}}{D_{h,l}^2\rho_l h_{fg} N H_g W_g}\right]\left[\sum_{m=1}^{\infty}\frac{A_m B_m \cos(B_m x)}{C_m \exp(B_m t_w) - D_m \exp(-B_m t_w)}\right]\end{aligned} \tag{8}$$

Integrating Eq. (8) with $u_l(0) = u_l(L_t - L_b) = 0$ determines the liquid pressure gradient and velocity:

$$\frac{dp_l}{dx} = \dot{Q}_{in}\left[\frac{4\mu_l (f\mathrm{Re})_l t_w \mathrm{Bi}_{eq}}{D_{h,l}^2\rho_l h_{fg} N H_g W_g}\right]\left[\sum_{m=1}^{\infty}\frac{A_m \sin(B_m x)}{C_m \exp(B_m t_w) - D_m \exp(-B_m t_w)}\right] \tag{9}$$

$$u_l = -\dot{Q}_{in}\left[\frac{2t_w \mathrm{Bi}_{eq}}{\rho_l h_{fg} N H_g W_g}\right]\left[\sum_{m=1}^{\infty}\frac{A_m \sin(B_m x)}{C_m \exp(B_m t_w) - D_m \exp(-B_m t_w)}\right] \tag{10}$$

Like the liquid flow, the vapor flow is assumed to be one-dimensional, fully developed, and incompressible. The vapor flow is considered as flow between parallel plates. As such, the axial vapor velocity is related to the pressure gradient using conservation of momentum:

$$u_v = -\frac{H_v^2}{12\mu_v}\frac{\mathrm{d}p_v}{\mathrm{d}x} \tag{11}$$

where $\mathrm{d}p_v/\mathrm{d}x$ is the vapor pressure gradient. Like the liquid velocity, the vapor velocity gradient is found from continuity:

$$\frac{\mathrm{d}u_v}{\mathrm{d}x} = \frac{4\mathrm{Bi}_{eq}(k_w/t_w) W_t\left[\Delta T(x,0)\right]}{\rho_v h_{fg} H_v W_v} \tag{12}$$

Combining Eqs. (11) and (12) yields:

$$\begin{aligned}\frac{\mathrm{d}^2 p_v}{\mathrm{d}x^2} &= -\frac{48\mu_v \mathrm{Bi}_{eq}(k_w/t_w) W_t\left[\Delta T(x,0)\right]}{\rho_v h_{fg} H_v^3 W_v} \\ &= -\dot{Q}_{in}\left[\frac{48\mu_v t_w \mathrm{Bi}_{eq}}{H_v^3 W_v \rho_v h_{fg}}\right]\left[\sum_{m=1}^{\infty}\frac{A_m B_m \cos(B_m x)}{C_m \exp(B_m t_w) - D_m \exp(-B_m t_w)}\right]\end{aligned} \tag{13}$$

Integrating Eq. (13) with $u_v(0) = u_v(L_t - L_b) = 0$ determines the vapor pressure gradient and velocity:

$$\frac{\mathrm{d}p_v}{\mathrm{d}x} = -\dot{Q}_{in}\left[\frac{48\mu_v t_w \mathrm{Bi}_{eq}}{H_v^3 W_v \rho_v h_{fg}}\right]\left[\sum_{m=1}^{\infty}\frac{A_m \sin(B_m x)}{C_m \exp(B_m t_w) - D_m \exp(-B_m t_w)}\right] \tag{14}$$

$$u_v = \dot{Q}_{in}\left[\frac{4t_w \mathrm{Bi}_{eq}}{H_v W_v \rho_v h_{fg}}\right]\left[\sum_{m=1}^{\infty}\frac{A_m \sin(B_m x)}{C_m \exp(B_m t_w) - D_m \exp(-B_m t_w)}\right] \tag{15}$$

Equations (10) and (15) are used to determine the remaining velocity ratio term, $|u_v/u_l|$, required to calculate $(f\mathrm{Re})_l$ in Eq. (6a):

$$\left|\frac{u_v}{u_l}\right| = \frac{2\rho_l N H_g W_g}{\rho_v H_v W_v} \tag{16}$$

Equation (16) can also be derived from continuity, given the identical boundary conditions used in the derivations of Eqs. (9), (10), (14), and (15).

The meniscus radius of curvature is related to the capillary pressure by the Young–Laplace equation [48,49]:

$$p_{cap} = p_v - p_l = \frac{\gamma_{lv}}{r_{cap}} = \gamma_{lv} K \tag{17}$$

where p_{cap}, r_{cap}, and K are the capillary pressure, meniscus (capillary) radius, and curvature, respectively. A heat pipe exhibits a maximum capillary pressure at the beginning of the evaporator and a minimum capillary pressure at the start of the liquid block [32]. It is commonly assumed that the minimum capillary pressure is set by the hydraulic radius of the vapor core [23]. In the present model, the minimum capillary pressure is assumed to be negligible, $p_{cap}(L_t - L_b) = 0$. As such, the axial capillary pressure can be found using Eqs. (9) and (14):

$$\begin{aligned}p_{cap} = p_v - p_l &= \int\left(\frac{\mathrm{d}p_v}{\mathrm{d}x} - \frac{\mathrm{d}p_l}{\mathrm{d}x}\right)\mathrm{d}x \\ &= \dot{Q}_{in}\left[\frac{4t_w \mathrm{Bi}_{eq}}{h_{fg}}\right]\left[\frac{12\mu_v}{H_v^3 W_v \rho_v} + \frac{\mu_l (f\mathrm{Re})_l}{D_{h,l}^2 \rho_l N H_g W_g}\right] \\ &\times \left[\sum_{m=1}^{\infty}\frac{(A_m/B_m)\left\{\cos(B_m x) - \cos\left[B_m(L_t - L_b)\right]\right\}}{C_m \exp(B_m t_w) - D_m \exp(-B_m t_w)}\right]\end{aligned} \tag{18}$$

Equations (17) and (18) determine the meniscus curvature used to model the evaporating and condensing films in Sections 2.2 and 2.3.

2.2. Evaporation

As shown in Fig. 3, the evaporating film is modeled as three regions: (i) the adsorbed film, where significant adhesion suppresses evaporation; (ii) the thin film, where a submicron film enables high evaporation rates; and (iii) the meniscus, where negligible adhesion, relative to cohesion, forms a constant curvature meniscus.

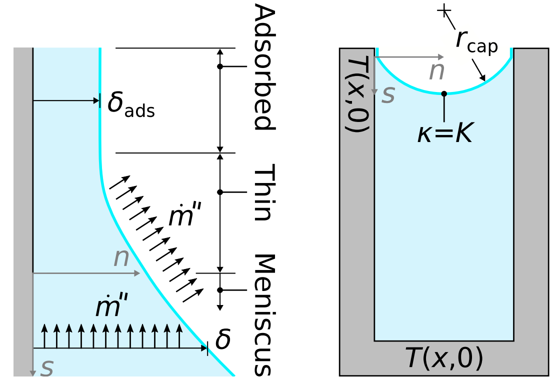

Fig. 3. Evaporating film in a groove. The evaporating film is modeled as three regions in the present study: the adsorbed film, thin film, and meniscus.

2.2.1. Thin film

The molecular attraction between the thin film and the solid substrate is significant. This attraction further decreases the liquid pressure in the Young–Laplace equation, Eq. (17). As such, it is accounted for by augmenting the Young–Laplace equation [50]:

$$p_v - p_l = p_d + p_{cap} \tag{19}$$

where p_d is the disjoining pressure. The disjoining pressure is commonly modeled with the following expression [33,50,51]:

$$p_d = \frac{A}{\delta^3} \tag{20}$$

where A and δ are the dispersion constant and film thickness, respectively. The capillary pressure is determined by the film curvature:

$$p_{cap} = \gamma_{lv}\kappa \tag{21}$$

where κ is the film curvature, which is determined using the curvature equation:

$$\kappa = \frac{\mathrm{d}^2\delta}{\mathrm{d}s^2}\left[1 + \left(\frac{\mathrm{d}\delta}{\mathrm{d}s}\right)^2\right]^{-3/2} \tag{22}$$

where s is local the coordinate parallel to the groove wall, as shown in Fig. 3. In the thin film, disjoining pressure is commonly modeled as more significant than capillary pressure [52,53]. As such, Eq. (19) can be simplified and combined with Eq. (20) which yields:

$$p_v - p_l = p_d + p_{cap} \approx p_d = \frac{A}{\delta^3} \tag{23}$$

The one-dimensional liquid mass flow rate in the film is related to the pressure gradient using a laminar boundary layer approximation (lubrication theory) [50]:

$$\dot{m}' = \rho_l \int_0^{\delta} w_l\,\mathrm{d}n = -\frac{\delta^3}{3\nu_l}\frac{\mathrm{d}p_l}{\mathrm{d}s} \tag{24}$$

where $\dot{m}'$, w_l, and $\mathrm{d}p_l/\mathrm{d}s$ are the mass flow rate per unit length, transverse liquid velocity, and liquid pressure gradient, respectively. The vapor pressure is assumed to be constant in the thin film region. As such, differentiating Eq. (23) and then combining the result with Eq. (24) yields [52,53]:

$$\dot{m}' = -\frac{A}{\nu_l}\frac{1}{\delta}\frac{\mathrm{d}\delta}{\mathrm{d}s} \tag{25}$$

where $\mathrm{d}\delta/\mathrm{d}s$ is the film thickness slope. For a steady-state thin film, continuity implies that the mass flux is as follows [52,53]:

$$\dot{m}'' = -\frac{\mathrm{d}\dot{m}'}{\mathrm{d}s} = \frac{A}{\nu_l}\frac{\mathrm{d}}{\mathrm{d}s}\left(\frac{1}{\delta}\frac{\mathrm{d}\delta}{\mathrm{d}s}\right) \tag{26}$$

The evaporative mass flux is also governed by kinetic theory [50,54]:

$$\dot{m}'' = a\left(T_{lv} - T_v\right) + b\left(p_l - p_v\right) \tag{27a}$$

where T_{lv} is the liquid–vapor interfacial temperature. The coefficients a and b are expressed as [50,54]:

$$a = \frac{2\sigma}{2-\sigma}\left(\frac{M}{2\pi R T_{lv}}\right)^{1/2}\left(\frac{p_v M h_{fg}}{R T_{lv} T_v}\right) \approx \frac{2\sigma}{2-\sigma}\left(\frac{M}{2\pi R T_v}\right)^{1/2}\left(\frac{p_v M h_{fg}}{R T_v^2}\right)$$

$$b = a\left(\frac{T_v}{\rho_l h_{fg}}\right) \tag{27b}$$

where σ, M, and R are the accommodation coefficient (taken in this study as unity, i.e., $\sigma = 1$), molecular weight, and universal gas constant, respectively. Neglecting the suppression due to disjoining and capillary pressure, the evaporative mass flux in Eq. (27) is simplified as follows [53]:

$$\dot{m}'' = a\left(T_{lv} - T_v\right) + b\left(p_l - p_v\right) \approx a\left(T_{lv} - T_v\right) \tag{28}$$

The conductive heat flux through the film is equal to the evaporative heat flux at the liquid–vapor interface, which yields:

$$\frac{k_l\left[T(x,0) - T_{lv}\right]}{\delta} = \dot{m}'' h_{fg} \tag{29}$$

Equations (28) and (29) are combined to eliminate T_{lv} as follows:

$$\dot{m}'' = \frac{a k_l\left[\Delta T(x,0)\right]}{k_l + a h_{fg}\delta} \tag{30}$$

Combining Eqs. (26) and (30) yields the following [53]:

$$\frac{A}{\nu_l}\frac{\mathrm{d}}{\mathrm{d}s}\left(\frac{1}{\delta}\frac{\mathrm{d}\delta}{\mathrm{d}s}\right) = \frac{a k_l\left[\Delta T(x,0)\right]}{k_l + a h_{fg}\delta} \tag{31}$$

which can be solved for the ratio of the thin film slope to thickness [52,53]. The total heat transfer rate per unit length in the thin film region is then determined using the total mass flow rate per unit length in Eq. (25), yielding the following for N grooves [53]:

$$\dot{Q}'_{thin} = 2N\left[\frac{2Aah_{fg}^2\left[\Delta T(x,0)\right]}{\nu_l}\ln\left(\frac{k_l}{a h_{fg}\delta_{ads}} + 1\right)\right]^{1/2} \tag{32a}$$

where δ_{ads} is the adsorbed film thickness which is approximated by setting $\dot{m}'' = 0$ in Eq. (27):

$$\delta_{ads} = \left(\frac{b}{a}\frac{A}{T_{lv} - T_v}\right)^{1/3} \approx \left(\frac{b}{a}\frac{A}{\left[\Delta T(x,0)\right]}\right)^{1/3} \tag{32b}$$

2.2.2. Meniscus

As discussed in Section 2.1, the meniscus radius of curvature is determined by the hydrodynamics and is constant at each axial location. Thus, the curvature equation in Eq. (22) can be written as:

$$\kappa = K = \frac{1}{r_{cap}} = \frac{\mathrm{d}^2\delta}{\mathrm{d}s^2}\left[1 + \left(\frac{\mathrm{d}\delta}{\mathrm{d}s}\right)^2\right]^{-3/2} \tag{33}$$

In the meniscus region, disjoining pressure is assumed to be negligible. Thus, Eq. (33) governs the meniscus film thickness distribution as:

$$\frac{\mathrm{d}^2\delta}{\mathrm{d}s^2} = K\left[1 + \left(\frac{\mathrm{d}\delta}{\mathrm{d}s}\right)^2\right]^{3/2} \tag{34}$$

Equation (34) is often simplified by assuming a negligible meniscus film slope, $\mathrm{d}\delta/\mathrm{d}s \approx 0$ [55–57]. The present model accounts for this slope while instead approximating for analytical solvability:

$$\frac{\mathrm{d}^2\delta}{\mathrm{d}s^2} = K\left[1 + \left(\frac{\mathrm{d}\delta}{\mathrm{d}s}\right)^2\right]^{3/2} \approx K\left[1 + \left(\frac{\mathrm{d}\delta}{\mathrm{d}s}\right)^2\right] \tag{35a}$$

The boundary conditions for the meniscus film thickness distribution are as follows:

$$\delta(0) = \delta_0, \qquad \left.\frac{\mathrm{d}\delta}{\mathrm{d}s}\right|_{s=0} = \tan\theta, \qquad \delta(l) = W_g/2 \tag{35b}$$

where the starting film thickness, δ_0, is found using Eq. (20) and a negligible disjoining pressure relative to the capillary pressure, $p_d|_{\delta=\delta_0} \approx p_{cap} \times 10^{-5}$ [33]. Equation (35) has the following analytical solution with the specified boundary conditions:

$$\delta = \delta_0 + K^{-1}\ln\left[\frac{\cos\theta}{\cos(Ks + \theta)}\right] \tag{36}$$

In the meniscus region, the liquid–vapor interfacial temperature is assumed to be equal to the vapor temperature, $T_{lv} \approx T_v$. The total heat transfer rate per unit length can be found using this temperature approximation in Eq. (29) and integrating. This yields the following for N grooves:

$$\dot{Q}'_{men} = 2Nk_l\left[\Delta T(x,0)\right]\int_0^l \delta^{-1}\,\mathrm{d}s \tag{37a}$$

where l is the modeled length of the meniscus film determined by the boundary condition in Eq. (35b):

$$l = K^{-1}\left(\cos^{-1}\left\{\frac{\cos\theta}{\exp\left[K\left(W_g/2 - \delta_0\right)\right]}\right\} - \theta\right) \tag{37b}$$

Figure 4 illustrates the meniscus of a grooved wick heat pipe near the capillary limit [25]. The present model's approximation for the meniscus film thickness distribution in Eq. (36) agrees with the exact solution for constant curvature well past the micro-region, where the majority of heat transfer occurs [58,59]. Also, as shown in Table 1, the present model for the total meniscus heat transfer rate per unit length in Eq. (37) agrees with the mathematical and numerical models of Do et al. [33] and Stephan and Busse [58], respectively. Modeling conditions can be found in [33,58] and are tabulated in Table A.1 of Appendix A. Agreement in thickness distribution and total heat transfer rate ascertain the validity of the present meniscus model in Eqs. (36) and (37).

Finally, the average heat transfer coefficient in the evaporator is found by summing the total heat transfer rate in the thin film and meniscus regions:

$$\bar{h}_e = \left(2L_e W_t\right)^{-1}\int_0^{L_e}\frac{\dot{Q}'_{thin} + \dot{Q}'_{men}}{\left[\Delta T(x,0)\right]}\,\mathrm{d}x \tag{38}$$

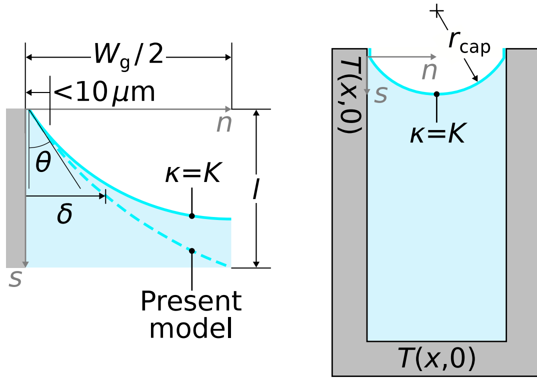

Fig. 4. Meniscus in a groove. The meniscus near the capillary limit for a grooved wick heat pipe is shown [25].

Table 1
Comparison of the total meniscus evaporation heat transfer rate per unit length with prior models. Modeling conditions are identical and can be found in [33,58], as tabulated in Table A.1 of Appendix A.

	$\dot{Q}'_{men}$ [W m^{-1}]
Stephan and Busse [58]	16.5
Do et al. [33]	18.0
Present model, Eq. (37)	16.5

2.3. Condensation

As shown in Fig. 5, the condensing film is modeled as two regions: (i) a thin film atop the fins, referred to as the fin film in this study, and (ii) a meniscus of constant curvature.

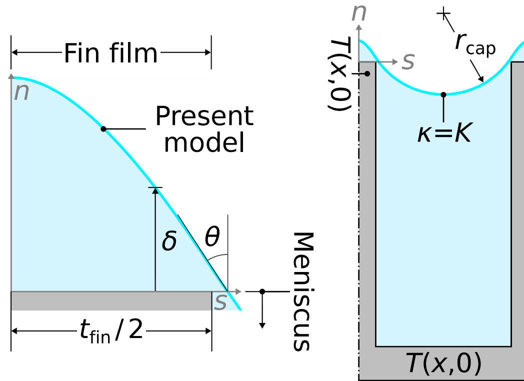

Fig. 5. Condensing film atop the fins and in the grooves. The condensing film is modeled as two regions in the present study: the thin film atop the fins, referred to as the fin film in the present study, and the meniscus.

2.3.1. Fin film

The thin film atop the fins, referred to as the fin film in this study, is assumed to have a negligible film thickness slope, $d\delta/ds \approx 0$. As such, the augmented Young–Laplace equation in Eq. (19) using Eqs. (21) and (22), becomes:

$$p_v - p_l = \frac{A}{\delta^3} + \gamma_{lv}\frac{d^2\delta}{ds^2}\left[1 + \left(\frac{d\delta}{ds}\right)^2\right]^{-3/2} \approx \frac{A}{\delta^3} + \gamma_{lv}\frac{d^2\delta}{ds^2} \tag{39}$$

where s is the local coordinate parallel to the groove wall, as shown in Fig. 5. In the fin film, the disjoining pressure gradient is assumed to be negligible relative to the capillary pressure gradient $dp_{cap}/ds \gg dp_d/ds$ [23,33]. Also, like in the thin film modeling in Section 2.2.1, the vapor pressure is assumed to be constant. As such, the liquid pressure gradient found from Eq. (39) is as follows:

$$\frac{dp_l}{ds} = -\gamma_{lv}\frac{d^3\delta}{ds^3} \tag{40}$$

Lubrication theory and continuity in Eqs. (24) and (26), respectively, relate the condensing mass flux to the film thickness distribution:

$$\dot{m}'' = -\frac{d\dot{m}'}{ds} = -\frac{d}{ds}\left(-\frac{\delta^3}{3\nu_l}\frac{dp_l}{ds}\right) = \frac{\gamma_{lv}}{3\nu_l}\frac{d}{ds}\left(\delta^3\frac{d^3\delta}{ds^3}\right) \tag{41}$$

Kinetic theory, the opposite of its simplified form in Eq. (30), also governs the condensing mass flux. Equating the opposite of Eq. (30) and (41) yields the following fourth-order governing equation for the fin film thickness distribution [33,53]:

$$\frac{\gamma_{lv}}{3\nu_l}\frac{d}{ds}\left(\delta^3\frac{d^3\delta}{ds^3}\right) = -\frac{ak_l\left[\Delta T(x,0)\right]}{k_l + ah_{fg}\delta} \tag{42}$$

where, with the following boundary conditions [23,33]:

$$\left.\frac{d\delta}{ds}\right|_{s=0} = \left.\frac{d^3\delta}{ds^3}\right|_{s=0} = 0, \qquad \left.\frac{d^2\delta}{ds^2}\right|_{s=0} = K, \qquad \left.\frac{d\delta}{ds}\right|_{s=t_{fin}/2} = -\tan\left(\frac{\pi}{2} - \theta\right) \tag{43}$$

the approximate solution is [23,33]:

$$\delta(s) = C_0 + C_1\left(s - t_{fin}/2\right) + C_2\left(s - t_{fin}/2\right)^2 + C_3\left(s - t_{fin}/2\right)^3 + C_4\left(s - t_{fin}/2\right)^4 \tag{44a}$$

with the following coefficients:

$$C_1 = -\tan(\pi/2 - \theta), \qquad C_2 = K/2, \qquad C_3 = 2C_4 t_{fin}, \qquad C_4 = \frac{C_2 - C_1 t_{fin}}{t_{fin}^3} \tag{44b}$$

The remaining coefficient, C_0, is determined by assuming that the total condensed mass flow rate is solely in the fin film, $0 \le s \le t_{fin}/2$. The total mass flow rate is found from the evaporator as follows:

$$\dot{m} = \frac{1}{h_{fg}}\int_0^{L_e} \dot{Q}'_{thin} + \dot{Q}'_{men}\, dx \tag{45}$$

where the total evaporative heat transfer rates per unit length in the thin film and meniscus regions, $\dot{Q}'_{thin}$ and $\dot{Q}'_{men}$, are found in Sections 2.2.1 and 2.2.2, more specifically, Eqs. (32) and (37), respectively. Integrating the mass flux in Eq. (41) and equating this to the total mass flow rate in Eq. (45) yields:

$$C_0 = \left[\nu_l\dot{m}\left(2\gamma_{lv}\int_{L_e+L_a}^{L_c-L_b} C_3\, dx\right)^{-1}\right]^{1/3} \tag{46}$$

The total heat transfer in the fin film is found by integrating the mass flux found from kinetic theory across the top of the fin [33]:

$$\dot{Q}'_{fin} = -h_{fg}\int_0^{t_{fin}/2} \dot{m}''\, ds = h_{fg}\int_0^{t_{fin}/2} \frac{ak_l\left[\Delta T(x,0)\right]}{k_l + ah_{fg}\delta}\, ds \tag{47}$$

Determining the total heat transfer rate for the condensing meniscus is identical to the derivation for the evaporating meniscus in Section 2.2.2, where it can be found using the opposite of Eq. (37). The average heat transfer coefficient in the condenser can finally be found by summing the total heat transfer rate in the fin film and meniscus regions as follows:

$$\bar{h}_c = \left[2\left(L_c - L_b\right)W_t\right]^{-1}\int_{L_e+L_a}^{L_c-L_b} \frac{\dot{Q}'_{fin} + \dot{Q}'_{men}}{\left[\Delta T(x,0)\right]}\, dx \tag{48}$$

2.4. Determination of the equivalent heat transfer coefficient

For simplicity, the equivalent heat transfer coefficient is taken in this study as the length-weighted average of the average heat transfer coefficients determined for the condenser and evaporator in Sections 2.2 and 2.3, more specifically, Eqs. (38) and (48), respectively, which yields:

$$h_{\mathrm{eq}} = \frac{L_{\mathrm{e}}\overline{h}_{\mathrm{e}} + (L_{\mathrm{c}} - L_{\mathrm{b}})\overline{h}_{\mathrm{c}}}{(L_{\mathrm{c}} - L_{\mathrm{b}}) + L_{\mathrm{e}}} \tag{49}$$

2.5. Solution procedure

Figure 6 outlines the solution procedures for the outer wall temperature and maximum heat transfer rate. Compared to prior numerical models, the present algorithm is computationally simple and does not involve solving a highly discretized system of coupled differential equations. Instead, the present algorithm involves basic computations, easily performed within seconds using any numeric computing platform on a typical workstation. After inputting the relevant conditions, the present model initializes the equivalent heat transfer coefficient by assuming only conduction through the liquid-filled groove into the vapor core:

$$\left(h_{\mathrm{eq}}\right)_{\mathrm{init.}} = \frac{k_{\mathrm{l}}}{H_{\mathrm{g}}} \tag{50}$$

Then, the inner temperature difference, $\Delta T\left(x,0\right)$, is determined using the analytical solution in Eq. (4). This temperature difference determines a re-calculated equivalent heat transfer coefficient using Eq. (49) and the evaporation and condensation sub-models in Sections 2.2 and 2.3, specifically Eqs. (38) and (48), respectively. If the difference between successive equivalent heat transfers is within the convergence criteria, which in the present study is 0.1%, the outer wall temperature distribution, $T_{\mathrm{w}}(x)$, is found by evaluating the temperature distribution in Eq. (3) at $y = t_{\mathrm{w}}$. If the convergence criterion is not met, the inner temperature difference is re-calculated based on the re-calculated equivalent heat transfer coefficient, and the loop continues. For the heat pipes investigated in the present study, it was found that the temperature loop, which calculates the inner temperature difference and the wall temperatures, tends to converge within five iterations. As previously mentioned, since the present model relies only on analytical and semi-analytical solutions, computational run times are within seconds, far quicker than those involved in implementing mathematical models such as the model of Do et al. [33], which requires a complex algorithm to numerically solve many coupled differential equations.

Determining the maximum heat transfer rate requires an additional outer loop that adjusts the heat power input until the capillary limit is reached. The capillary limit is determined by the maximum capillary pressure, $p_{\mathrm{cap}}\left(0\right)$, which is found by evaluating the capillary pressure in Eq. (18) at $x = 0$. The theoretical maximum capillary pressure is governed by the minimum capillary radius and the Young–Laplace equation in Eq. (17):

$$\begin{aligned} r_{\mathrm{cap,min}} &= \frac{W_{\mathrm{g}}}{2\cos\theta} \\ p_{\mathrm{cap,max}} &= \frac{\gamma_{\mathrm{lv}}}{r_{\mathrm{cap,min}}} \end{aligned} \tag{51}$$

If the difference between the calculated and theoretical maximum capillary pressures in Eqs. (18) and (51), respectively, is within 0.1%, the maximum heat transfer rate, $\dot{Q}_{\mathrm{max}}$, is found as the input heat transfer rate, $\dot{Q}_{\mathrm{in}}$. If not, the loop of adjusting $\dot{Q}_{\mathrm{in}}$ continues. For the heat pipes investigated in the present study, it was found that the maximum heat transfer rate loop tends to converge within five iterations.

3. Results and discussion

3.1. Model validation

The present model is validated with copper–water grooved heat pipes using the numerical data of Do et al. [33] and the experimental data of Hopkins et al. [25] and Lin et al. [60]. Heat pipe specifications, namely operating conditions, dimensions, and properties, are tabulated in Table B.1 of Appendix B. Figure 7 compares the present model to that of Do et al. [33] and the experimental data of Lin et al. [60]. The present model differs by less than 4% in wall temperature, average evaporator wall temperature, and average condenser wall temperature compared to the experimental data. The present model also shows close agreement with the numerical data.

Figure 8 compares the present model to the model of Do et al. [33] and the experimental data of Hopkins et al. [25]. The present model differs by less than 2% in wall temperatures at specific locations in the evaporator and condenser compared to experimental data and closely agrees with the numerical data. Figure 8b shows that the maximum heat transfer rate predicted by the present model differs by less than 10% compared to the experimental data for varying vapor temperature and, again, closely agrees with the numerical data. The present model shows significantly closer agreement to the experimental data than the closed-form model of Hopkins et al. [25] in Eq. (1), which differs by more than 30%. The present model accurately predicts the experimentally determined wall temperatures and maximum heat transfer rates available for grooved heat pipes in the literature.

3.2. Parametric analysis

An experimental copper–water heat pipe [25], referred to as the baseline, is parametrically analyzed using the present model. The baseline specifications for the heat pipe are found in Table B.1 of Appendix B. The studied parameters include the water contact angle, wall thermal conductivity, and groove width and height.

3.2.1. Wall thermal conductivity and water contact angle

The water contact angle, or wetting angle, measures how well water wets the solid surface. A lower water contact angle results in a lower minimum capillary radius and, thus, a higher maximum heat transfer rate for the heat pipe. There are several methods to enhance the wettability of copper. These include chemical treatment and surface oxidation [61] and plasma treatments [62,63], to list a few. Like Prysiazhnyi et al. [62] reported for a plasma-treated copper surface, surfaces tend to revert to their pre-treated elevated contact angles. There is a need to analyze the effect of wetting angle on heat pipe performance to determine if a potentially short-lived lower wetting angle-induced performance enhancement is worthwhile. Alternatively, different wall materials, such as ceramics with inherently lower wetting angles than copper, have been explored for heat pipes due partly to their sustained enhanced wettability [64–67]. Although ceramics can exhibit lower wetting angles than copper, they have lower thermal conductivity. There is a need for a parametric analysis of the effect of wall thermal conductivity and wetting angle on the thermal performance of a heat pipe. Figure 9 shows the effect of wall thermal conductivity and wetting angle on the maximum heat transfer rate and the thermal resistance of the baseline heat pipe. Thermal resistance is defined as follows:

$$R = \frac{\overline{T}_{\mathrm{w,e}} - \overline{T}_{\mathrm{w,c}}}{\dot{Q}_{\mathrm{in}}} \tag{52}$$

where $\overline{T}_{\mathrm{w,e}}$ and $\overline{T}_{\mathrm{w,c}}$ are the average wall temperatures in the evaporator and condenser, respectively. The reported thermal resistance is at its minimum value, which is when $\dot{Q}_{\mathrm{in}} = \dot{Q}_{\mathrm{max}}$. The results indicate that a high wall thermal conductivity and low wetting angle are preferred to maximize the maximum heat transfer rate and minimize the minimum thermal resistance. A higher wall thermal conductivity lowers the wall

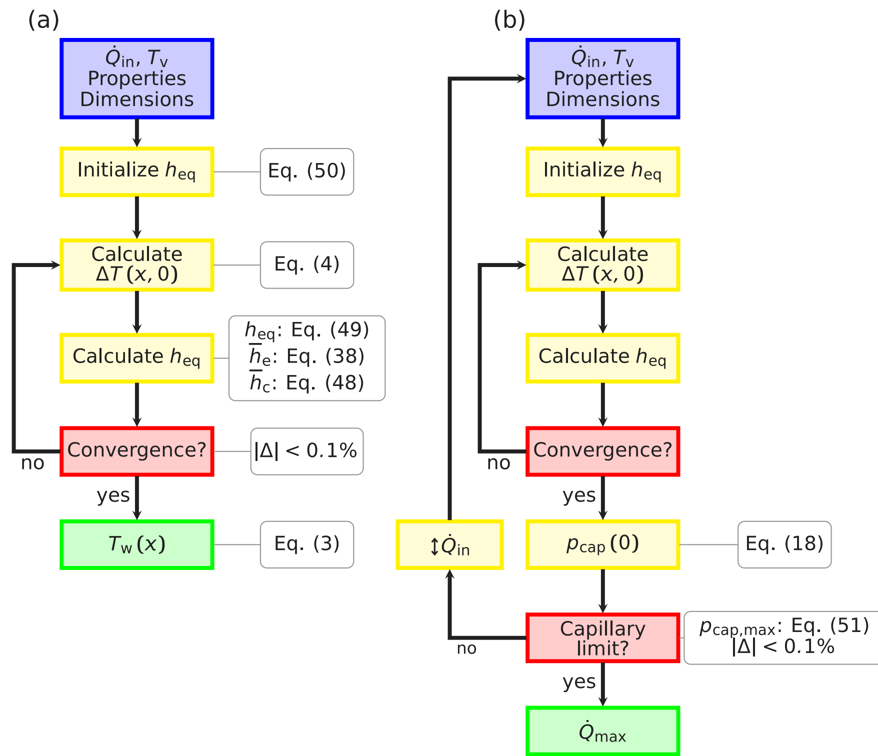

Fig. 6. Solution procedure to determine the (a) wall temperature and (b) maximum heat transfer rate. Determining the maximum heat transfer rate requires an outer loop that adjusts the heat power input until the capillary limit is reached. A complete list of the required inputs for the present model can be found in Table B.1 of Appendix B.

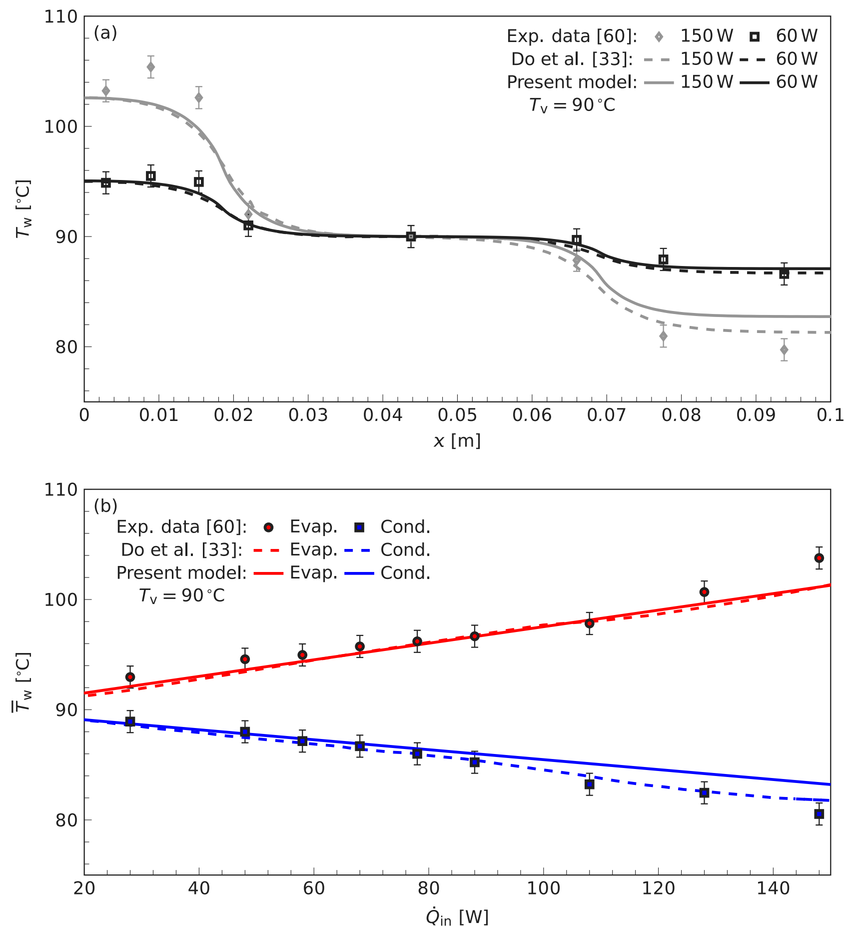

Fig. 7. Present model validation with numerical [33] and experimental data [60]: (a) wall temperature distribution and (b) average evaporator and condenser wall temperatures.

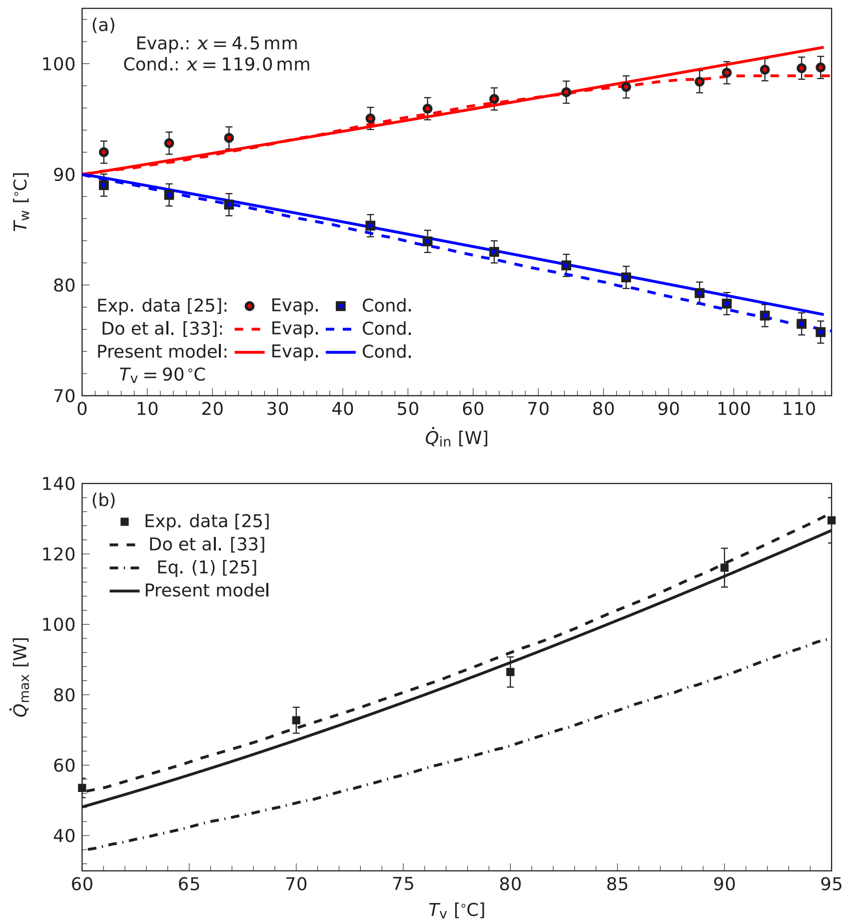

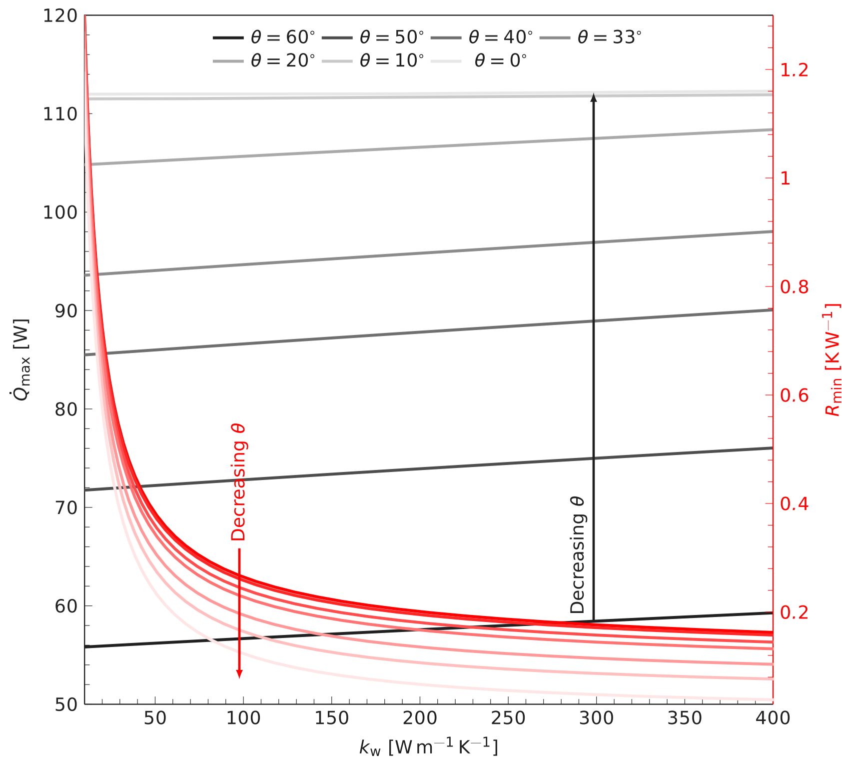

Fig. 8. Present model validation with numerical [33] and experimental data [25]: (a) evaporator and condenser wall temperatures and (b) maximum heat transfer rate. The present model is also compared to the closed-form model of Hopkins et al. [25] in Eq. (1).

Fig. 9. The effect of wall thermal conductivity and water contact angle on the maximum heat transfer rate and the minimum thermal resistance of the heat pipe in [25].

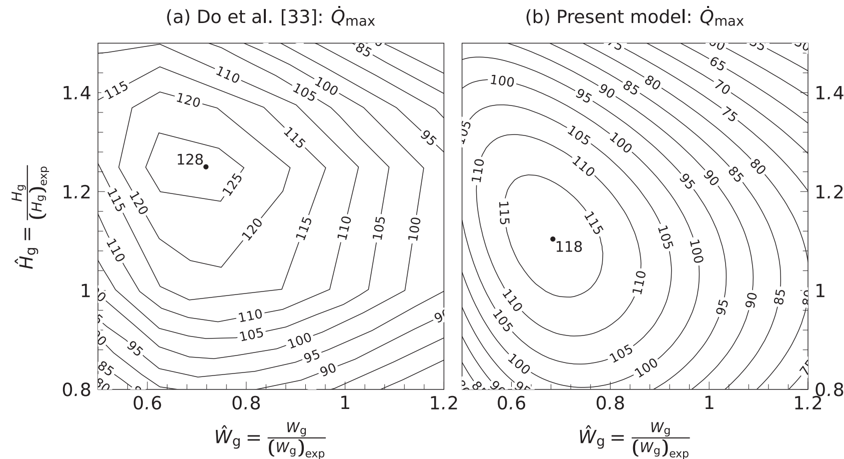

Fig. 10. The effect of varying groove width and height on the maximum heat transfer rate of the heat pipe in [25]. The results of (a) a previous mathematical model [33] and (b) the present model. Groove width and height are normalized to their baseline values.

conductive thermal resistance while promoting axial wall conduction as an additional heat path. A lower wetting angle lowers the meniscus film's conductive thermal resistance while increasing the capillary limit. For the baseline copper surface ($k_w = 400\,\mathrm{W\,m^{-1}\,K^{-1}}$, $\theta = 33°$), the present model finds that lowering the wetting angle increases the maximum heat transfer rate by up to 15% for the considered baseline heat pipe. Lowering the wetting angle also reduces the minimum thermal resistance by up to 71%. Additionally, the present model finds that varying wall thermal conductivity while maintaining the wetting angle does not significantly change the maximum heat transfer rate. For example, reducing the wall thermal conductivity to $10\,\mathrm{W\,m^{-1}\,K^{-1}}$, representing a 40-fold reduction from the baseline, reduces the maximum heat transfer rate by less than 5% for $\theta = 33°$. However, such a wall thermal conductivity reduction leads to a significant increase in the minimum thermal resistance, with the present model reporting a staggering increase of more than 800%. Maintaining the same reduced wall thermal conductivity (i.e., $k_w = 10\,\mathrm{W\,m^{-1}\,K^{-1}}$), the present model reports a relatively marginal reduction in the minimum thermal resistance of up to 10% by lowering the wetting angle. These results indicate that although reducing the wall thermal conductivity only marginally reduces the maximum heat transfer rate, it considerably increases the minimum thermal resistance, making any potential reductions by lowering the wetting angle insignificant. As such, the present model indicates that wall thermal conductivity can be a more significant determining factor when considering alternative heat pipe wall materials than wetting angle.

3.2.2. Groove dimensions

In addition to the varying wall thermal conductivity and water contact angle analysis, varying groove dimensions, namely width and height, are studied. Reducing width while maintaining height and the number of grooves increases the capillary limit but reduces liquid cross-sectional area, leading to a higher liquid pressure drop. Increasing height while maintaining width, wall thickness, and overall heat pipe thickness increases the liquid cross-sectional area, reducing the liquid pressure drop but also reduces the vapor cross-sectional area, leading to a higher vapor pressure drop. These trade-offs highlight the need to parametrically analyze the effect of groove dimensions on the maximum heat transfer rate of grooved heat pipes.

Figure 10 shows the maximum heat transfer rates predicted by the model of Do et al. [33] and the present model for varying groove width and height. Results are reasonably consistent between the models, further validating the present model. Groove width and height are normalized to their baseline values as tabulated in Table B.1 of Appendix B. Vapor temperature, wall thickness, number of grooves, and lengths of the heat pipe (evaporator, condenser, and total) are maintained as their values tabulated in Table B.1 of Appendix B. Since thermal resistance is minimized in the absence of a liquid block [33], the liquid block length is chosen to be zero. The results indicate that a slightly narrower and deeper groove is preferred for this specific baseline heat pipe to maximize its maximum heat transfer rate. The previous model finds the optimum width and height to be 0.144 and 0.525 mm (−28 and +25% compared to the baseline), respectively [33], while the present model finds these values to be 0.137 and 0.464 mm (−32 and +10% compared to the baseline), respectively. Both models indicate theoretical enhancements in the maximum heat transport of about 20% compared to the baseline heat pipe.

4. Conclusions

A compact mathematical model is developed to predict axial variations of the wall temperature and the maximum heat transfer rate of a flat micro heat pipe with a rectangular grooved wick. Along with dimensional quantities, such as groove and vapor widths and heights, the present model accounts for vapor temperature, liquid–vapor interfacial shear stress, contact angle, and fill volume. The present model uses the analytical solution to the two-dimensional conduction equation in the wall and an equivalent heat transfer coefficient. The equivalent heat transfer coefficient is determined using an iterative method that considers analytical and semi-analytical models for evaporation and condensation heat transfer rates. This computationally efficient iterative method can also provide a framework for modeling other grooved or porous wick heat pipes for which analytical or semi-analytical solutions to the wall conduction, fluid flow, and film equations exist. Given the non-discretized nature of the present model, computations on most workstations can be completed within seconds, making it compelling for use in parametric and optimization studies. The present model closely agrees with published numerical and experimental results for wall temperatures and maximum heat transfer rates. A previously investigated heat pipe is parametrically analyzed using the present model with respect to its wall thermal conductivity, water contact angle, and groove width and height. The present model found that the maximum

heat transfer rate of the heat pipe can be enhanced by about 15 and 20% by varying its wetting angle and groove dimensions, respectively.

CRediT authorship contribution statement

Callum Chhokar: Conceptualization, Methodology, Investigation, Validation, Writing – original draft. **Mahyar Ashouri:** Conceptualization, Methodology, Investigation, Validation, Writing – review & editing. **Majid Bahrami:** Supervision, Funding acquisition, Writing – review & editing.

Declaration of competing interest

The authors declare that they have no known competing financial interests or personal relationships that could have appeared to influence the work reported in this paper.

Data availability

Data will be made available on request.

Acknowledgments

The authors gratefully acknowledge the financial support of the Natural Sciences and Engineering Research Council of Canada (NSERC), 2023-581192. The authors also gratefully acknowledge Michael Nikkhoo and Kiarash Vakhshouri for their support and guidance in conceptualizing this publication.

Appendix A. Conditions for the meniscus evaporation heat transfer rates in Table 1

The conditions in Table A.1 were used to calculate the total meniscus evaporation heat transfer rates in Table 1. Complete lists of the conditions can be found in [33,58].

Table A.1
Conditions used to calculate the total meniscus evaporation heat transfer rates that are compared in Table 1.

ΔT [K]	1.31
A [J]	2×10^{-21}
W_g [m]	1×10^{-3}
r_{cap} [m]	9.091×10^{-4}
α [°]	45
θ [°]	19.7
k_l [W m^{-1} K^{-1}]	0.48
h_{fg} [J kg^{-1}]	1180×10^3

Appendix B. Specifications of the experimental heat pipes

The heat pipe specifications in Table B.1, namely operating conditions, dimensions, and properties were used in the model validation and parametric analysis, Sections 3.1 and 3.2, respectively. The remaining working temperature-dependent properties were taken from widely available tabulated data. Copper's water contact angle was taken from Stepanov et al. [68]. Liquid block length, L_b, in Table B.1 is calculated from the liquid fill volume as follows (maintaining consistent units):

$$L_b = \frac{\text{Liquid fill} \times (\rho_l)_{T_{fill}} - N W_g H_g L_t \times (\rho_l)_{T_v} - W_v H_v L_t \times (\rho_v)_{T_v}}{W_v H_v \times \left[(\rho_l)_{T_v} - (\rho_v)_{T_v}\right]} \quad \text{(B.1)}$$

Table B.1
Specifications of the experimental heat pipes used in the model validation and parametric analysis. The table lists all of the required model inputs except working temperature-dependent fluid properties which were taken from widely available tabulated data in the present study.

	Hopkins et al. [25]	Lin et al. [60]
W_t [mm]	13.41	12.70
W_v [mm]	9.70	10.26
H_v [mm]	1.22	2.13
t_w [mm]	3.43	1.27
W_g [mm]	0.200	0.203
H_g [mm]	0.420	0.839
t_{fin} [mm]	0.100	0.102
N [ea.]	62	64
L_t [mm]	120.0	101.6
L_e [mm]	15.6	18.5
L_c [mm]	34.4	32.5
L_b [mm]	19.0–20.6	0
$\dot{Q}_{in}$ [W]	0–120	0–150
T_v [°C]	60–95	90
Liquid fill [mL]	0.84	0.87
Wall	Copper	Copper
k_w [W m^{-1} K^{-1}]	400	400
Fluid	Water	Water
θ [°]	33	33

References

[1] The International Roadmap for Devices and Systems (IRDS) - more Moore, IEEE, 2022.

[2] A. Bar-Cohen, J.J. Maurer, D.H. Altman, Embedded cooling for wide bandgap power amplifiers: A review, J. Electron. Packag. Trans. ASME 141 (4) (2019) 1–14, http://dx.doi.org/10.1115/1.4043404.

[3] J. Ditri, M.K. McNulty, S. Igoe, S3-P10: Embedded microfluidic cooling of high heat flux electronic components, in: Lester Eastman Conference 2014 - High Performance Devices, LEC 2014, 2014, pp. 0–3, http://dx.doi.org/10.1109/LEC.2014.6951565.

[4] J. Ditri, J. Hahn, R. Cadotte, M. McNulty, D. Luppa, Embedded cooling of high heat flux electronics utilizing distributed microfluidic impingement jets, in: ASME 2015 International Technical Conference and Exhibition on Packaging and Integration of Electronic and Photonic Microsystems, InterPACK 2015, Collocated with the ASME 2015 13th International Conference on Nanochannels, Microchannels, and Minichannels, Vol. 3, 2015, pp. 1–10, http://dx.doi.org/10.1115/IPACK2015-48689.

[5] L.T. Su, S. Naffziger, M. Papermaster, Multi-chip technologies to unleash computing performance gains over the next decade, in: 2017 IEEE International Electron Devices Meeting, IEDM, 2017, p. 1, http://dx.doi.org/10.1109/IEDM.2017.8268306.

[6] The International Roadmap for Devices and Systems (IRDS) - Systems and Architectures, IEEE, 2022.

[7] W. Gomes, A. Koker, P. Stover, D. Ingerly, S. Siers, S. Venkataraman, C. Pelto, T. Shah, A. Rao, F. O'Mahony, E. Karl, L. Cheney, I. Rajwani, H. Jain, R. Cortez, A. Chandrasekhar, B. Kanthi, R. Koduri, Ponte vecchio: A multi-tile 3D stacked processor for exascale computing, in: IEEE International Solid-State Circuits Conference, IEEE, 2022, pp. 42–44, http://dx.doi.org/10.1109/ISSCC42614.2022.9731673.

[8] T.P. Cotter, Principles and prospects for micro heat pipes, in: Proceedings of the 5th International Heat Pipe Conference, 1984, pp. 328–335.

[9] T. Liu, M.T. Dunham, K.W. Jung, B. Chen, M. Asheghi, K.E. Goodson, Characterization and thermal modeling of a miniature silicon vapor chamber for die-level heat redistribution, Int. J. Heat Mass Transfer 152 (2020) 119569, http://dx.doi.org/10.1016/j.ijheatmasstransfer.2020.119569.

[10] T. Liu, M. Asheghi, K.E. Goodson, Performance and manufacturing of silicon-based vapor chambers, Appl. Mech. Rev. 73 (1) http://dx.doi.org/10.1115/1.4049801.

[11] S. Launay, V. Sartre, M. Lallemand, Experimental study on silicon micro-heat pipe arrays, Appl. Therm. Eng. 24 (2–3) (2004) 233–243, http://dx.doi.org/10.1016/j.applthermaleng.2003.08.003.

[12] Z. Wang, Y. Song, J. Yang, H. Yu, B. Jiao, X. Yu, The visualized investigation of a silicon based built-in heat pipe micropillar wick structure, Appl. Therm. Eng. 144 (2018) 1117–1125, http://dx.doi.org/10.1016/j.applthermaleng.2018.08.060.

[13] S. Saygan, Y. Akkus, Z. Dursunkaya, B. Cetin, Capillary boosting for enhanced heat pipe performance through bifurcation of grooves: Numerical assessment and experimental validation, Int. Commun. Heat Mass Transfer 137 (March) http://dx.doi.org/10.1016/j.icheatmasstransfer.2022.106162.

[14] B. Li, X. Yin, W. Tang, J. Zhang, Optimization design of grooved evaporator wick structures in vapor chamber heat spreaders, Appl. Therm. Eng. 166, http://dx.doi.org/10.1016/j.applthermaleng.2019.114657.

[15] F. Yao, S.S. Miao, M. Zhang, Y. Chen, An experimental study of an anti-gravity vapor chamber with a tree-shaped evaporator, Appl. Therm. Eng. 141 (2018) 1000–1008, http://dx.doi.org/10.1016/j.applthermaleng.2018.06.053.

[16] W. Liu, Y. Peng, T. Luo, Y. Luo, K. Huang, The performance of the vapor chamber based on the plant leaf, Int. J. Heat Mass Transfer 98, http://dx.doi.org/10.1016/j.ijheatmasstransfer.2016.02.091.

[17] E. Sadeghinezhad, M. Mehrali, M.A. Rosen, A.R. Akhiani, S. Tahan Latibari, M. Mehrali, H.S.C. Metselaar, Experimental investigation of the effect of graphene nanofluids on heat pipe thermal performance, Appl. Therm. Eng. 100 (2016) 775–787, http://dx.doi.org/10.1016/j.applthermaleng.2016.02.071.

[18] H. Hassan, S. Harmand, 3D transient model of vapour chamber: Effect of nanofluids on its performance, Appl. Therm. Eng. 51 (1–2) (2013) 1191–1201, http://dx.doi.org/10.1016/j.applthermaleng.2012.10.047.

[19] M. Kole, T.K. Dey, Thermal performance of screen mesh wick heat pipes using water-based copper nanofluids, Appl. Therm. Eng. 50 (2013) 763–770, http://dx.doi.org/10.1016/j.applthermaleng.2012.06.049.

[20] X. Wang, Q. Wen, J. Wu, J. Yang, X. Zhao, Z. Wang, A novel neural network and sensitivity analysis method for predicting the thermal resistance of heat pipes with nanofluids, Appl. Therm. Eng. 236, http://dx.doi.org/10.1016/j.applthermaleng.2023.121677.

[21] B.R. Babin, G.P. Peterson, D. Wu, Steady-state modeling and testing of a micro heat pipe, J. Heat Transfer 112 (3) (1990) 595–601, http://dx.doi.org/10.1115/1.2910428.

[22] D. Wu, G.P. Peterson, Investigation of the transient characteristics of a micro heat pipe, J. Thermophys. Heat Transfer 5 (2) (1991) 129–134, http://dx.doi.org/10.2514/3.239.

[23] D. Khrustalev, A. Faghri, Thermal analysis of a micro heat pipe, J. Heat Transfer 116 (1) http://dx.doi.org/10.1115/1.2910855.

[24] D. Khrustalev, A. Faghri, Thermal characteristics of conventional and flat miniature axially grooved heat pipes, J. Heat Transfer 117 (4) (1995) 1048–1054, http://dx.doi.org/10.1115/1.2836280.

[25] R. Hopkins, A. Faghri, D. Khrustalev, Flat miniature heat pipes with micro capillary grooves, J. Heat Transfer 121 (1) (1999) 102–109, http://dx.doi.org/10.1115/1.2825922.

[26] C. Yue, Q. Zhang, Z. Zhai, L. Ling, CFD simulation on the heat transfer and flow characteristics of a microchannel separate heat pipe under different filling ratios, Appl. Therm. Eng. 139 (2018) 25–34, http://dx.doi.org/10.1016/j.applthermaleng.2018.01.011.

[27] X. Wang, Y. Zhu, Y. Wang, Development of pressure-based phase change model for CFD modelling of heat pipes, Int. J. Heat Mass Transfer 145 (2019) 118763, http://dx.doi.org/10.1016/j.ijheatmasstransfer.2019.118763.

[28] V. Guichet, B. Delpech, H. Jouhara, Experimental investigation, CFD and theoretical modeling of two-phase heat transfer in a three-leg multi-channel heat pipe, Int. J. Heat Mass Transfer 203, http://dx.doi.org/10.1016/j.ijheatmasstransfer.2022.123813.

[29] W.Z. Fang, Y.Q. Tang, C. Yang, W.Q. Tao, Numerical simulations of the liquid-vapor phase change dynamic processes in a flat micro heat pipe, Int. J. Heat Mass Transfer 147 (2020) 119022, http://dx.doi.org/10.1016/J.IJHEATMASSTRANSFER.2019.119022.

[30] G. Gökçe, C. Kurt, G. Odabaşı, Z. Dursunkaya, B. Çetin, Comprehensive three-dimensional hydrodynamic and thermal modeling of steady-state operation of a flat grooved heat pipe, Int. J. Multiph. Flow 160 (2023) 104370, http://dx.doi.org/10.1016/J.IJMULTIPHASEFLOW.2022.104370.

[31] G. Gökçe, B. Çetin, Z. Dursunkaya, Accelerated 3D CFD modeling of multichannel flat grooved heat pipes, Energy 305 (2024) 132289, http://dx.doi.org/10.1016/J.ENERGY.2024.132289.

[32] S.J. Kim, J.K. Seo, K.H. Do, Analytical and experimental investigation on the operational characteristics and the thermal optimization of a miniature heat pipe with a grooved wick structure, Int. J. Heat Mass Transfer 46 (11) (2003) 2051–2063, http://dx.doi.org/10.1016/S0017-9310(02)00504-5.

[33] K.H. Do, S.J. Kim, S.V. Garimella, A mathematical model for analyzing the thermal characteristics of a flat micro heat pipe with a grooved wick, Int. J. Heat Mass Transfer 51 (19–20) (2008) 4637–4650, http://dx.doi.org/10.1016/j.ijheatmasstransfer.2008.02.039.

[34] F. Lefèvre, R. Rullière, G. Pandraud, M. Lallemand, Prediction of the temperature field in flat plate heat pipes with micro-grooves - experimental validation, Int. J. Heat Mass Transfer 51 (15–16) http://dx.doi.org/10.1016/j.ijheatmasstransfer.2007.12.007.

[35] S. Saygan, Y. Akkus, Z. Dursunkaya, B. Çetin, Fast and predictive heat pipe design and analysis toolbox: H-pat, Isi Bilim. Teknigi Derg./ J. Therm. Sci. Technol. 42 (1) (2022) 141–156, http://dx.doi.org/10.47480/isibted.1107492.

[36] R.S. Prasher, A simplified conduction based modeling scheme for design sensitivity study of thermal solution utilizing heat pipe and vapor chamber technology, J. Electron. Packag. Trans. ASME 125 (3) (2003) 378–385, http://dx.doi.org/10.1115/1.1602479.

[37] S. Zimmermann, R. Dreiling, T. Nguyen-Xuan, M. Pfitzner, An advanced conduction based heat pipe model accounting for vapor pressure drop, Int. J. Heat Mass Transfer 175 (2021) 121014, http://dx.doi.org/10.1016/j.ijheatmasstransfer.2021.121014.

[38] F. Lefèvre, M. Lallemand, Coupled thermal and hydrodynamic models of flat micro heat pipes for the cooling of multiple electronic components, Int. J. Heat Mass Transfer 49 (7–8) (2006) 1375–1383, http://dx.doi.org/10.1016/j.ijheatmasstransfer.2005.10.001.

[39] S. Lips, F. Lefèvre, A general analytical model for the design of conventional heat pipes, Int. J. Heat Mass Transfer 72 (2014) 288–298, http://dx.doi.org/10.1016/j.ijheatmasstransfer.2013.12.068.

[40] P.D. Dunn, D.A. Reay, Heat Pipes, fourth ed., Pergamon, New York, NY, 1994.

[41] A. Faghri, Heat Pipe Science and Technology, first ed., Taylor & Francis, 1994.

[42] S. Chi, Heat Pipe Theory and Practice: A Sourcebook, McGraw-Hill, New York, NY, 1976.

[43] F. Lefèvre, S. Lips, J. Bonjour, Investigation of evaporation and condensation processes specific to grooved flat heat pipes, Front. Heat Pipes 1 (2) http://dx.doi.org/10.5098/fhp.v1.2.3001.

[44] H. Carslaw, J. Jaeger, Conduction of Heat in Solids, Clarendon Press; Oxford University Press, 1959.

[45] G.E. Schneider, R. DeVos, Non-Dimensional Analysis for the Heat Transport Capability of Axially Grooved Heat Pipes Including Liquid/Vapor Interaction, AIAA Paper No. 80-021, http://dx.doi.org/10.2514/6.1980-214.

[46] J.P. Longtin, B. Badran, F.M. Gerner, A one-dimensional model of a micro heat pipe during steady-state operation, J. Heat Transfer 116 (3) (1994) 709–715, http://dx.doi.org/10.1115/1.2910926.

[47] Frank M. White, Viscous Fluid Flow, McGraw-Hill, 1991.

[48] T. Young III, An essay on the cohesion of fluids, Philos. Trans. R. Soc. Lond. 95 (1805) 65–87, http://dx.doi.org/10.1098/rstl.1805.0005.

[49] P. Laplace, Supplement to the tenth edition, Méch. Célest. 10.

[50] P.C. Wayner, Y.K. Kao, L.V. LaCroix, The interline heat-transfer coefficient of an evaporating wetting film, Int. J. Heat Mass Transfer 19 (5) (1976) 487–492, http://dx.doi.org/10.1016/0017-9310(76)90161-7.

[51] B.V. Derjaguin, Z.M. Zorin, Optical study of the adsorption and surface condensation of vapours in the vicinity of saturation on a smooth surface, Prog. Surf. Sci. 40 (1–4) http://dx.doi.org/10.1016/0079-6816(92)90037-I.

[52] J.A. Schonberg, P.C. Wayner, An analytical solution for the integral contact line evaporative heat sink, J. Thermophys. Heat Transfer 6 (1) (1992) 128–134, http://dx.doi.org/10.2514/6.1990-1787.

[53] H. Wang, S.V. Garimella, J.Y. Murthy, An analytical solution for the total heat transfer in the thin-film region of an evaporating meniscus, Int. J. Heat Mass Transfer 51 (25–26) (2008) 6317–6322, http://dx.doi.org/10.1016/J.IJHEATMASSTRANSFER.2008.06.011.

[54] P.C. Wayner Jr., The effect of interfacial mass transport on flow in thin liquid films, Colloids Surf. 52 (C) (1991) 71–84, URL http://www.scopus.com/inward/record.url?eid=2-s2.0-0026060309&partnerID=40&md5=050cabcb8304a02f45dc463caca00df7.

[55] K.P. Hallinan, H.C. Chebaro, S.J. Kim, W.S. Chang, Evaporation from an extended meniscus for nonisothermal interfacial conditions, J. Thermophys. Heat Transfer 8 (4) (1994) 709–716, http://dx.doi.org/10.2514/3.602.

[56] S. DasGupta, J.A. Schonberg, P.C. Wayner, Investigation of an evaporating extended meniscus based on the augmented young-laplace equation, J. Heat Transfer 115 (1) http://dx.doi.org/10.1115/1.2910649.

[57] K. Park, K.J. Noh, K.S. Lee, Transport phenomena in the thin-film region of a micro-channel, Int. J. Heat Mass Transfer 46 (13) http://dx.doi.org/10.1016/S0017-9310(02)00541-0.

[58] P.C. Stephan, C.A. Busse, Analysis of the heat transfer coefficient of grooved heat pipe evaporator walls, Int. J. Heat Mass Transfer 35 (2) http://dx.doi.org/10.1016/0017-9310(92)90276-X.

[59] A.J. Jiao, H.B. Ma, J.K. Critser, Evaporation heat transfer characteristics of a grooved heat pipe with micro-trapezoidal grooves, Int. J. Heat Mass Transfer 50 (15–16) http://dx.doi.org/10.1016/j.ijheatmasstransfer.2007.01.009.

[60] L. Lin, R. Ponnappan, J. Leland, High performance miniature heat pipe, Int. J. Heat Mass Transfer 45 (15) (2002) 3131–3142, http://dx.doi.org/10.1016/S0017-9310(02)00038-8.

[61] J. Shi, X. Jia, D. Feng, Z. Chen, C. Dang, Wettability effect on pool boiling heat transfer using a multiscale copper foam surface, Int. J. Heat Mass Transfer 146 (2020) 118726, http://dx.doi.org/10.1016/j.ijheatmasstransfer.2019.118726.

[62] V. Prysiazhnyi, P. Slavicek, M. Cernak, Aging of plasma-activated copper and gold surfaces and its hydrophilic recovery after water immersion, Thin Solid Films 550, http://dx.doi.org/10.1016/j.tsf.2013.10.176.

[63] H.S. Salapare, J.A. Balbarona, L. Clerc, P. Bassoleil, A. Zenerino, S. Amigoni, F. Guittard, Cupric oxide nanostructures from plasma surface modification of copper, Biomimetics 4 (2) http://dx.doi.org/10.3390/biomimetics4020042.

[64] M.A. Zampino, Embedded Heat Pipes in Cofired Ceramic Substrates for Enhanced Thermal Management of Electronics (Ph.D. thesis), Florida International University, 2001, http://dx.doi.org/10.1201/9780203741771.

[65] M.A. Zampino, W.K. Jones, Embedded miniature heat pipes in ceramic cofire substrates, SAE Tech. Pap. 108 (1999) (1999) 8–13, http://dx.doi.org/10.4271/1999-01-1361.

[66] M.A. Zampino, W.K. Jones, Y. Cao, Substrate embedded heat pipes compatible with ceramic cofired processing, Int. J. Microcircuits Electron. Packag. 21 (1) (1998) 52–58.

[67] M. Gao, Y. Cao, M.A. Zampino, Ceramic miniature heat pipes and liquid charging methods, Heat Transf. Eng. 31 (7) (2010) 564–569, http://dx.doi.org/10.1080/01457630903425510.

[68] V.G. Stepanov, L.D. Volyak, Y.V. Tarlakov, Wetting contact angles for some systems, J. Eng. Phys. 32 (1977) 1000–1003.